Thermodynamic Stability and Anion Ordering of Perovskite Oxynitrides

Samuel D. Young,[†,‡] Jiadong Chen,[¶] Wenhao Sun,[*,¶] Bryan R. Goldsmith,[*,†] and Ghanshyam Pilania[*,§,‡]

†*Department of Chemical Engineering, University of Michigan, 2300 Hayward St., Ann Arbor, MI 48109, USA*
‡*Materials Science and Technology Division, Los Alamos National Laboratory, Los Alamos, NM, 87545, USA*
¶*Department of Materials Science, University of Michigan, 2300 Hayward St., Ann Arbor, MI 48109, USA*
§*Probabilistic Design and Materials Informatics Group, GE Research, Schenectady, NY 12309, USA*

E-mail: whsun@umich.edu; bgoldsm@umich.edu; ghanshyam.pilania@ge.com

Abstract

Perovskite oxynitrides (PONs) are a promising class of materials for applications ranging from catalysis to photovoltaics. However, the vast space of single PON materials ($ABO_{3-x}N_x$) has yet to be fully explored. Additionally, the community needs guidelines that relate PON chemistry and anion ordering to stability to better understand how to design PON materials that resist corrosion and decomposition under operating conditions. Screening this materials space requires identifying candidate PON materials that will be stable under operating conditions, which in turn requires methods to evaluate each material's stability. Here we predict the stability of single PON materials using a four-step approach based on density functional theory modeling: (i) enumerate viable cation pairs, (ii) select an energetically favorable prototypical anion ordering, (iii) compute each PON's free energy above the thermodynamic convex hull, and (iv) generate computational Pourbaix diagrams to determine allowable ranges of electrochemical operating conditions. A critical part of our approach is determining a prototypical stable anion ordering for both ABO_2N and $ABON_2$ stoichiometries across a variety of A- and B-site cations. We demonstrate a stable anion ordering containing a high degree of *cis* ordering between B cations and minority-composition anions. We predict 85 stable and 109 metastable PON compounds, with $A \in \{La, Pb, Nd, Sr, Ba, Ca\}$ and $B \in \{Re, Os, Nb, Ta\}$ forming cation pairs that lead to stable PONs less than 10 meV/atom above the thermodynamic convex hull. Computational Pourbaix diagrams for two stable candidates, $CaReO_2N$ and $LaTaON_2$, suggest that not all compounds with zero energy above the thermodynamic convex hull can be easily synthesized.

1 Introduction

Heteroanionic materials are a class of transition metal compounds in which metal cations coordinate with two or more anions. This class includes materials such as metal oxysulfides, metal oxynitrides, and metal oxyfluorides. Heteroanionic materials have several applications, including in energy storage as battery cathode materials,[1] in solid-state illumination as phosphor materials,[2] and in ammonia synthesis as electrocatalysts.[3] The heteroanionic material design space is vast owing to the many possible combinations of metal cations, anion choice, anion ordering, and lattice structures.[1] Perovskites are a subset of heteroanionic compounds characterized by at least two metal cations surrounded by anions arranged in octahedral geometries. Perovskite materials are well known for their applications in photovoltaics,[4] but have also been used for water splitting[5] and light-emitting diodes.[6]

Perovskite oxynitrides (PONs) are a special case of perovskite oxides in which the anion sites are occupied by either O or N, with the general single-PON formula $ABO_{3-x}N_x$, with $0 < x < 3$. Single PONs consist of 12-fold-coordinated A-site cations and 6-fold-coordinated B-site cations, with the B-site cations coordinated by octahedra of O or N anions that may arrange to form anion disorder, short-range order, or long-range order. Along with anion ordering and composition, the choice of A and B metal cations with multiple possible oxidation states creates a large combinatorial space for tuning the physical and electronic properties of these materials. At least 68 single PON materials have been synthesized, and many more potentially stable PONs have been predicted.[7]

Because the vast space of PON compounds has not yet been thoroughly explored, many promising material chemistries are likely unrealized. Understanding how chemical composition and anion ordering affect the stability of single PONs is critical to realize their synthesis and utility in several applications. Here we employ a density-functional-theory (DFT)-based, hierarchal down-selection approach to study PON stability across a wide compositional space of single PONs. We recognize that a full study of PONs would include the significantly larger design space of double and layered PONs, but for reasons of computational tractability we limit the scope of this work to the high tunability already possible in single PONs. This high compositional tunability may enable fine-tuning the physicochemical properties of these materials, making them useful for a variety of applications including electrochemical reactions,[3,8] photocatalysis,[9] photovoltaics,[10] and ionic semiconduction.[11] **Figure 1** shows our four-part approach for finding stable single PONs. To create a feasible search space, we begin by enumerating cation pairs likely to form stable PON structures using selected elements along with filtering rules to keep the number of DFT calculations feasible (**Figure 1a**). Second, we address the question of anion ordering by enumerating symmetrically distinct orderings of O^{2-} and N^{3-} within the single PON unit cell and evaluating their relative ground-
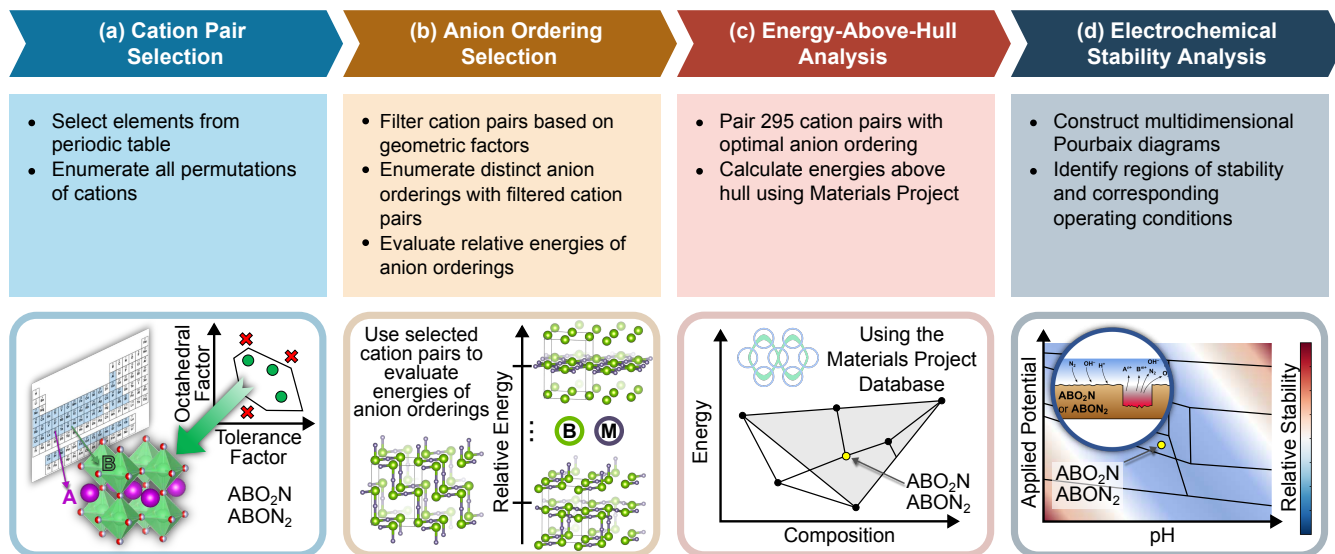
Figure 1. Workflow for identifying stable perovskite oxynitride compounds. The workflow involves four major steps: **(a)** cation pair selection, **(b)** anion ordering selection, **(c)** energy-above hull analysis, and **(d)** electrochemical stability analysis via computational Pourbaix diagrams.

state energies when paired with representative cation pairs (**Figure 1b**). Third, we combine the enumerated cation pairs and prototypical stable anion ordering determined in the first two steps to form a set of single PON compounds. For each single PON compound, we calculate the energy above the thermodynamic convex hull as a metric of stability (**Figure 1c**). [12] Finally, we explore the stability of two selected PONs, $CaReO_2N$ and $LaTaON_2$, in aqueous electrochemical reactions by creating Pourbaix diagrams and mapping regions of electrochemical stability as a function of applied potential and pH (**Figure 1d**). Our workflow demonstrates that *cis* ordering of O and N anions around the $B(O,N)_6$ octahedra is preferred above *trans* ordering, consistent with literature reports of synthesized perovskite oxynitrides and oxysulfides. [13,14] Our screening identifies a set of 85 stable ($\leq$ 10 meV/atom) and 109 metastable ($>$ 10 meV/atom and $\leq$ 25 meV/atom) PONs, potentially tripling the space of known stable PON materials. The most stable compositions involve La, Pb, Nd, Sr, Ba, or Ca as the A-site cation and Re, Os, Nb, or Ta as the B-site cation. Evaluating the stability of $CaReO_2N$ and $LaTaON_2$ shows that while both are stable with regard to decomposition to other solid compounds, only $LaTaON_2$ is also stable under reasonable aqueous electrochemical operating conditions.

2 Methods

All DFT calculations were performed using the Vienna Ab Initio Simulation Package (VASP), version 5.4.4. [15–18] Calculation preparation and post-processing were done using the Atomic Simulation Environment [19] (version 3.17) and Pymatgen [20] (version 2020.1.28) libraries. Unless otherwise noted, all calculations used the same VASP settings used in the Materials Project (as implemented in the MPRelaxSet class in Pymatgen) to compare results with the Materials Project database. [21] The projector-augmented wave method and associated pseudopotentials were used to describe core electrons, [22,23] and the PBE exchange-correlation functional was used. [24] Calculations

were spin-polarized, with plane waves expanded in a basis set up to 520 eV. *k* points were determined automatically according to the MPRelaxSet standard with a reciprocal *k* point density of 64 *k* points/Å^{-3} in reciprocal space. For each PON structure, we adjusted the ground-state energy to include corrections to oxide energies and GGA + *U* energies that are necessary to combine our ground-state energies with Materials Project data. [25,26] The PON structures were modeled using a $\sqrt{2} \times \sqrt{2} \times 2$ conventional unit cell with 20 atoms total. This conventional unit cell was taken from material mp-4019 of the Materials Project database ($CaTiO_3$, 0 meV/atom energy above hull) and idealized by rounding the fractional coordinates of all ions to integer multiples of 0.25. For bulk relaxations of PON structures, we used a tighter electronic tolerance (10^{-5} eV) compared to the Materials Project default (10^{-3} eV) to help some structures converge. Combined volume and ion position (i.e., ISIF = 3) relaxations were conducted at least two times to alleviate errors arising from Pulay stresses. Geometry relaxations proceeded using conjugate gradient or quasi-Newton force optimizers. Where necessary, VASP mixing parameters were adjusted and RMM-DIIS iterations were replaced with blocked Davidson iterations to ensure self-consistent electronic convergence. Anion orderings were obtained for a $\sqrt{2} \times \sqrt{2} \times 2$ PON supercell. The Enumlib software package was used to enumerate symmetrically distinct anion orderings. [27]

Five-dimensional computational Pourbaix diagrams were created for the Ca–Re–O–N–H and La–Ta–O–N–H systems. These many-component Pourbaix diagrams were constructed from the half-space intersection for all phases in each system, with the phase of lowest Pourbaix potential identified as the stable phase at the given conditions. [28,29] Ion energies are obtained from the Materials Project Pourbaix diagram framework. [30] Details of the Pourbaix potential derivation are provided in **Section S4**.

3 Results and Discussion

The four parts of our workflow in **Figure 1** filter the space of single PONs for stable candidates. **Section 3.1** discusses our enumeration of cation pairs, including classification of in-hull or out-of-hull status based on the Goldschmidt tolerance and octahedral factors. **Section 3.2** details this study's principal effort to improve the accuracy of stability predictions by identifying a prototypical anion ordering that is generally preferred across all cation chemistries. **Section 3.3** reports our screening process to identify stable PON structures by combining the cation pairs identified in **Section 3.1** and the anion ordering identified in **Section 3.2**. **Section 3.4** discusses using Pourbaix diagrams to further evaluate stability in the context of electrochemical reactions and highlights the need to supplementing general catalyst searches with application-specific screening.

3.1 Cation Pair Selection

As a first line of screening and to more clearly focus on the influence of cation chemistry and anion stoichiometry on stability, we focused on two PON compositions: ABO_2N and $ABON_2$. We selected A- and B-site cations from a set of 57 elements focusing on non-radioactive transition and post-transition metals, rare-earth metals, alkali metals, and alkaline metals (**Figure S1**). Allowable cation pairs were determined by enumerating pairs of A and B cations with nominal charges adding to +7 or +8 (i.e., to charge-balance the anions in ABO_2N or $ABON_2$ compositions, respectively), and for which A and B were not the same element. Pairs of cations with multiple oxidation states, such that given cation pair could add to both +7 and +8 charges, or to the same +7 or +8 charge in different ways, were counted as separate pairs. This enumeration process resulted in a set of 310 unique cation pairs. We note that a recent study by Wang et al.[7] investigating the stability of oxynitrides,

oxyfluorides, and nitrofluorides included a few Tc-containing oxynitride cation pairs not found by our enumeration process, specifically $Ba^{II}Tc^{V}O_2N$, $Ca^{II}Tc^{V}O_2N$, $Pb^{II}Tc^{V}O_2N$, $La^{III}Tc^{V}O_2N$, $Sr^{II}Tc^{V}O_2N$, and $La^{III}Tc^{IV}O_2N$. While our enumeration excludes radioactive elements, we include these six cation pairs for completeness and for comparison to that study, bringing the total number of unique cation pairs to 316.

Screening studies of perovskite structures often exploit geometric descriptors, such as the Goldschmidt tolerance[32] and octahedral[33] factors based on ionic radii, to predict whether a certain cation chemistry will lead to a stable perovskite structure. Proposed PON structures with Goldschmidt tolerance and octahedral factors close to those of known stable PONs are more likely to be stable. For each of the 316 unique proposed cation pairs and the 68 cation pairs of known stable PONs, we calculated the Goldschmidt tolerance[32] and octahedral[34] factors using geometric means of the ionic radii in each structure (**Table S1**). Ionic radii were obtained from a database of machine-learned ionic radii that account for the oxidation state of each ion.[35] The list of all cation pairs considered, with their Goldschmidt tolerance and octahedral factors, is given in **Table S2**.

The resulting data appear in **Figure 2a**, which displays a structure map for the proposed and known stable cation pairs. The 68 known stable cation pairs were used to form a convex hull shape against which we compare the 316 unique proposed cation pairs. To avoid confusion with the concept of a thermodynamic convex hull, we refer to the convex hull shape as the geometric hull. We consider a proposed PON with a certain cation pair stable according to geometric factors if its point on the structure map falls inside the geometric hull. Many proposed cation pair points cluster nearby or inside of the geometric hull, indicating that there may be many yet-undiscovered PONs that are experimentally stable. Of the 316 unique cation pairs, 90 (28.5%) fall within the geomet-
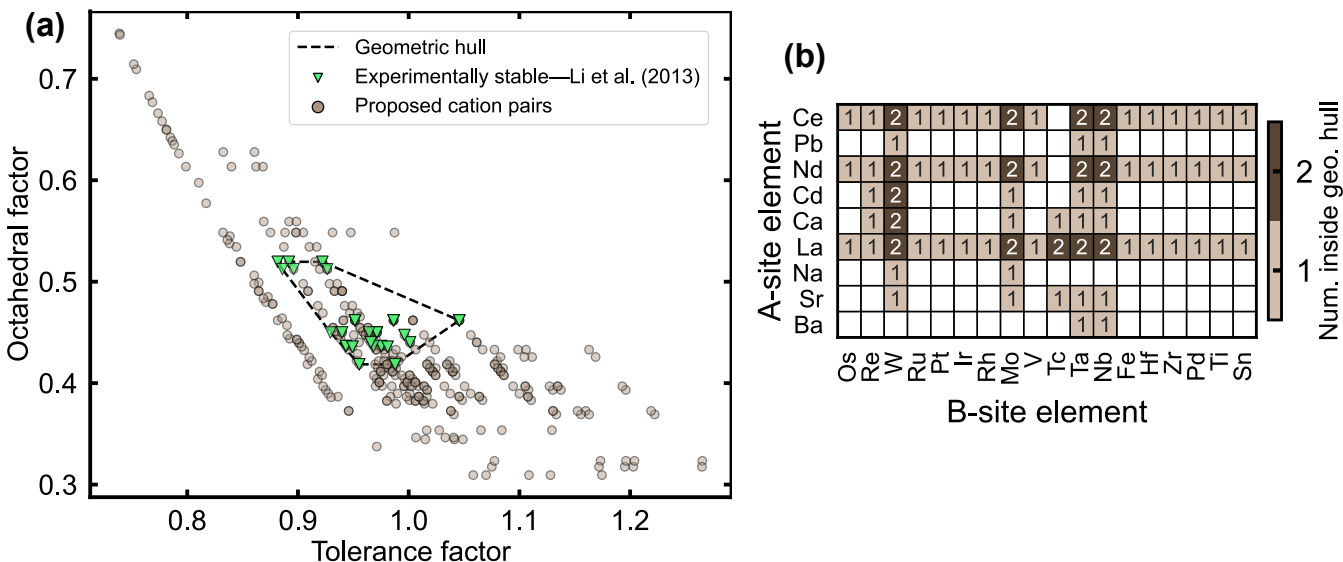

Figure 2. Perovskite oxynitride cation pairs predicted to fall within the geometric hull. (a) Structure map of Goldschmidt tolerance and octahedral factors for various single PON cation pairs. Experimentally stable points (green triangles) refer to PONs that have been synthesized and form an geometric hull (black dashed line).[31] Proposed cation pairs (brown circles) refer to the PONs that we screened for stability. **(b)** Heatmap showing the counts of proposed PON compounds that fall inside the geometric hull. Blank cells indicate that no proposed PON of that cation pair falls within the geometric hull. All cation pairs with a count of 1 are ABO_2N.

ric hull and 226 (71.5%) fall outside. Additionally, a number of points lie outside of but visually close to the geometric hull (i.e., within a perpendicular Euclidean distance of 0.02 units from an edge of the geometric hull). 28 of the 316 unique cation pairs fulfill this this criterion. We later explore the possibility that the true region of stability may be different than that enclosed by the hull of currently synthesized materials. The 90 points inside the geometric hull mostly represent compounds with $A \in \{Ce, Nd, La\}$ and $B \in \{Re, W, Mo, Ta, Nb\}$ (**Figure 2b**). In particular, many compounds with $A = La$ or $B = W$ are likely to be stable, according to the Goldschmidt tolerance and octahedral factors. Our first-pass analysis using only geometric factors identifies potential cation chemistries that lead to stable PONs. However, the many points outside of but close to the geometric hull suggest that some stable PONs might remain undiscovered using this method. This finding motivates a deeper evaluation of stability with consideration of a prototypical anion ordering.

3.2 Determination of prototypical anion ordering

We next address the question of which anion orderings are most stable in single PONs. Screening PONs is complicated by the possibility of many anion orderings and the potential for each unique cation pair to prefer a different anion ordering, making a DFT study of all possible combinations infeasible. Thus, the present study focuses on understanding how the preferred anion ordering changes as a function of cation charge configuration and identifying reasonable prototypical anion orderings that can be used for many structures at once. For heteroanionic perovskite systems of two anions in which the anions have the same charge but vastly different sizes, strain effects largely determine which anion orderings are preferred.[14] This is the expected behavior for perovskite oxysulfides, in which O^{2-} and S^{2-} are predicted to have effective Shannon ionic radii of 1.40 Å and 1.84 Å, respectively.[35] However, if the two anions have similar sizes but very different charges, then the preferred anion orderings are likely those that minimize the total electrostatic energy of the structure and will thus depend on the charges of the cations. We expect this latter behavior with PON systems, in which the respective Shannon ionic radii of O^{2-} and N^{3-} are 1.40 Å and 1.46 Å.

We propose that the dependence of anion order on cation choice can be modeled by ranking the ground-state energies of a series of PON structures, each with the same cation pair but different anion orderings. While it would be computationally infeasible to calculate the ground-state energies of all possible anion orderings with all 316 unique cation pairs, we can feasibly test all anion orderings combined with a limited set of cation pairs. We selected 16 unique cation pairs to use for anion ordering ranking, focusing on a subset of cation pairs that both (i) spans a range of charge configurations and (ii) spans a range of A and B cation radii. The selected charge configurations were $A^{I}B^{VI}$, $A^{II}B^{V}$, and $A^{III}B^{IV}$ for $ABON_2$; and $A^{II}B^{VI}$ and $A^{III}B^{V}$ for $ABON_2$. These criteria consider the effects both of cation charge (i.e., electrostatics) and cation size (i.e., strain effects) that might affect the preferred anion ordering. **Table S3** shows the list of cation pairs used for anion ordering analysis, along with their charges and ionic radii. We preferred cation pairs in which at least one of the cations had no more than one nominal oxidation state. The rationale behind this preference is that limiting the number of oxidation states reduces the number of cation pairs that could be matched with both ABO_2N and $ABON_2$ compositions, thus helping clearly distinguish the effect of PON composition on the preferred anion ordering.

To find possible anion orderings, we began with an ideal ABO_3 $\sqrt{2} \times \sqrt{2} \times 2$ perovskite structure and explored partial substitution of O^{2-} with N^{3-} anions, subject to the constraints that O^{2-} and N^{3-} compositions remain in a 2:1 ratio for ABO_2N or 1:2 ratio for $ABON_2$. We identify 32 symmetrically distinct anion orderings satisfying these constraints. These anion orderings are shown in **Figure S2** for ABO_2N and **Figure S3** for $ABON_2$. Because of the symmetry of the ABO_2N and $ABON_2$ compositions, the 32 anion orderings are the same between compositions except for the swapping of O^{2-} and N^{3-} anions.

We next combined each of the 16 unique cation pairs chosen for this analysis with each of the 32 anion orderings, choosing either the ABO_2N anion orderings for cation pairs adding to a charge of +7 or the $ABON_2$ anion orderings for cation pairs adding to a charge of +8. In total, we evaluated the ground-state energies of 512 structures. We calculate the ground-state energies using DFT rather than point-ion electrostatic models such as the Madelung energy[36] for reasons of accuracy (**Figure S7**). These calculations represent about 5% of the calculations needed to exhaustively determine the prototypical anion ordering for all 316 unique cation pairs discussed earlier. For each cation pair, the anion orderings were ranked in order of increasing energy (**Figures S8–S12** and **Tables S4–S8**), with the lowest-energy anion ordering for each cation pair assigned a ranking number of 1, the second-lowest a ranking number of 2, and so on. Cumulative rankings were calculated across all cation pairs tested by summing these ranking numbers and by summing the relative ground-state energies, leading to the prediction of one anion ordering in particular as most preferred on average over all cation pairs (**Figure S13**). We henceforth denote this first most preferred anion ordering, both in **Figure S13** and in the main text, as O_0, with the second most preferred anion ordering denoted O_1, and so on.

Figure 3 shows the O_0 anion ordering and key results of the anion ordering analysis. **Figure 3a–d** contains four different views of anion ordering O_0. **Figure 3a** shows a full O_0 PON structure which has an ABO_2N composition and arbitrary A and B cations. **Figure 3b** shows a $2 \times 2 \times 4$ supercell with an alternative view of the O_0 anion ordering focusing on the topology of M–B–M bonds between the B-site cation and the minority-composition (M) anion. **Figure 3c, d** shows the skeletal framework of B–(O, N) bonds for ABO_2N and $ABON_2$ compositions, respectively. These two structures are identical except for the swapping of O and N elements. **Figure 3e, f** show the cumulative rankings of O_0 and a few other anion orderings as measured by both place number and relative DFT energy across all 16 cation pairs used for anion ordering analysis. Both cumulative ranking metrics predict O_0 to be thermodynamically preferred over all other anion orderings, on average. Finally, **Figure 3g, h** shows how certain measures of the degree of M–B–M *cis* bonding relate to ground-state energy.

In PON structures where the compositions of each anion are not equal, changing the positions of M–B–M bonds will affect the degree of M–B–M *cis* bonding in the structure. The topology and degree of M–B–M *cis* bonding are important factors in

rationalizing why certain anion orderings are preferred in PON structures. The degree of *cis* ordering within each B-site octahedron has been shown to correlate to thermodynamic stability in other heteroanionic perovskite compounds. For example, a recent computational study that exhaustively evaluated all possible anion orderings of the metal oxysulfide $SrHf(O_{0.5}S_{0.5})_3$ predicted that the preferred anion ordering must have anions arranged in a *cis* configuration around the B-site cation.[14] This preferred ordering was rationalized in terms of competing electronic, electrostatic, and strain effects. Additionally, a neutron-

and electron-diffraction study of $SrBO_2N$ (B = Nb, Ta) PONs found that $SrBO_2N$ consistently prefers a partial anion ordering with –B–M– bonds forming *cis*-oriented chains within the equatorial planes of the BO_2N octahedra.[13] The present work tests the hypothesis that similar *cis* orderings are preferred for perovskite oxynitrides generally.

The preferred O_0 anion ordering contains many instances of *cis* bonding. To rationalize quantitatively the importance of *cis* bonding in PON compounds (and why some *cis*-ordered anion orderings are lower in energy than others), we calculated two
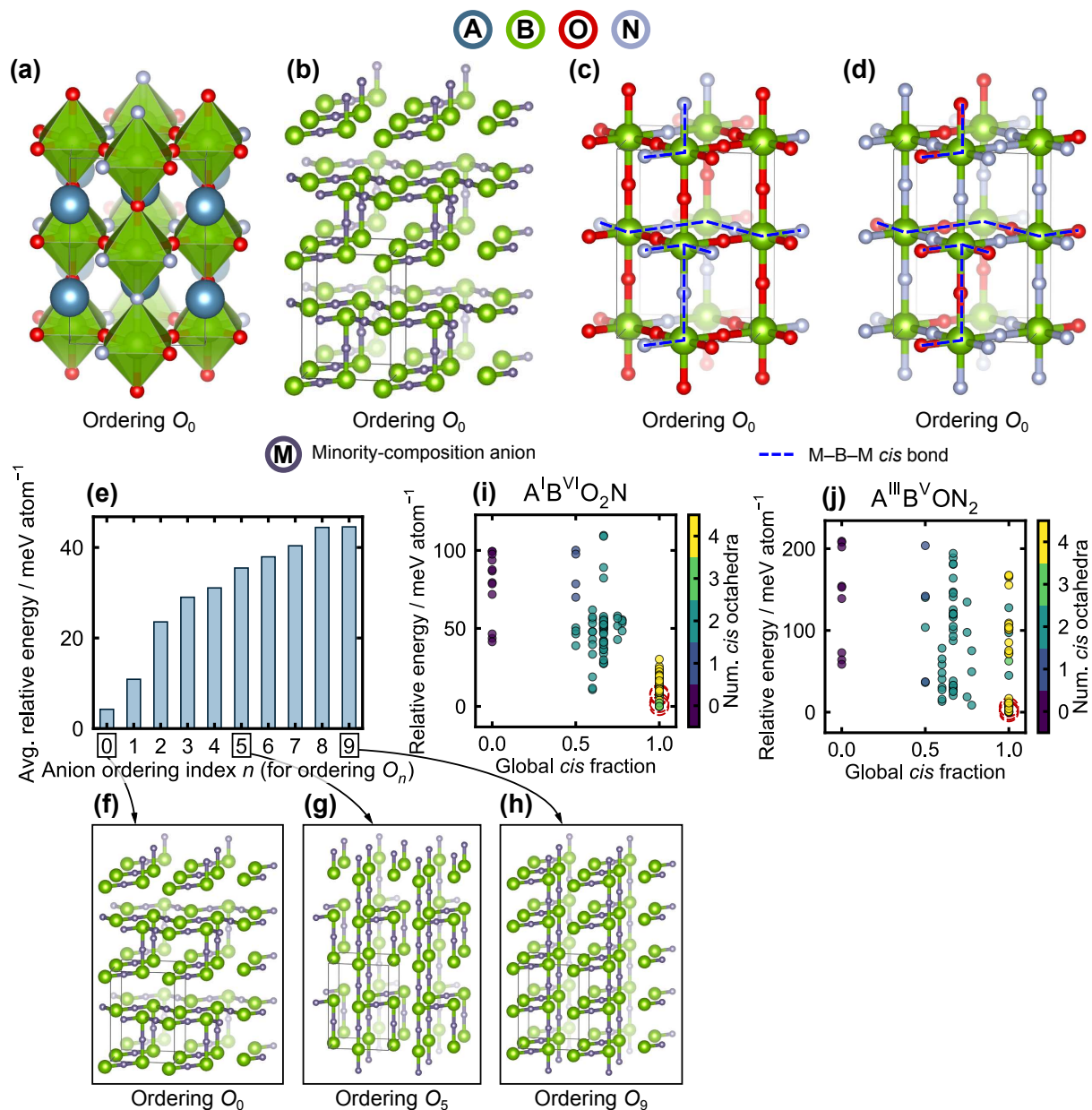

Figure 3. Rationalizing proposed anion ordering for general PON screening. (a) $\sqrt{2} \times \sqrt{2} \times 2$ supercells showing the full structure of our proposed prototypical, stable anion ordering O_0. **(b)** $2 \times 2 \times 4$ supercell showing the topology of the O_0 anion ordering with only the M–B–M bonds and no A-site cations. M (dark gray) is the minority-composition anion (i.e., N for ABO_2N and O for $ABON_2$). **(c, d)** $\sqrt{2} \times \sqrt{2} \times 2$ supercells showing the O_0 anion ordering, with A-site cations omitted for clarity, for **(c)** ABO_2N and **(d)** $ABON_2$ structures. Dotted lines overlay the M–B–M *cis* bonds. **(e)** Top 10 cumulative rankings by average ground-state energy for each anion ordering, across all 16 cation pairs tested and across all 32 symmetrically distinct anion orderings (**Figure S13**), with orderings O_0, O_5, and O_9 **(f–h)** shown for comparison. **(i, j)** Calculated relative DFT energy versus metrics of the amount of *cis* ordering for two representative cation charge configurations. Points surrounded by dotted red circles indicate the O_0 anion ordering (**Figure S6**).

simple metrics of the degree of *cis* bonding: the global fraction of *cis* bonding and the number of *cis* octahedra. For each anion ordering, the global fraction of *cis* bonding is calculated by counting all of the M–B–M bonds within a $\sqrt{2} \times \sqrt{2} \times 2$ supercell and determining which fraction of those bonds have a 90° angle through the B-site cation. The number of *cis* octahedra is calculated by counting how many of the four octahedra in a $\sqrt{2} \times \sqrt{2} \times 2$ supercell contain at least one *cis* M–B–M bond (**Figures S4** and **S5**). These metrics were chosen to measure not just how often M–B–M *cis* bonding occurs in an anion ordering, but also whether anion orderings with M–B–M *cis* bonds distributed throughout the structure are preferred about those with such bonds concentrated in one part of the structure. **Figure 3g, h** shows these metrics for all 32 anion orderings when combined with cation pairs of charge configurations $A^{III}B^{V}$ and $A^{I}B^{VI}$, respectively, with data for the remaining charge configurations shown in **Figure S6**. Although there is too much variance in the relative ground-state energies of each anion ordering to state strong quantitative correlations, some trends exist. The points near global *cis* fractions of 0.0, 0.6, and 1.0 form three general clusters. The point at the bottom of each cluster indicates the anion ordering leading to the minimum possible ground-state energy for a certain global *cis* fraction, similar to a thermodynamic convex hull plot. As the global *cis* fraction increases, the bottom point of each cluster becomes lower in energy, indicating that a higher fraction of *cis* bonds enables lower-energy anion orderings. A similar relationship exists between the relative ground-state energy and the number of *cis* octahedra. The clusters at a 0.0 global *cis* fraction tend to be composed of anion orderings with *cis* bonds distributed across zero or one octahedra. The clusters at a 0.6 global *cis* fraction generally have anion orderings with *cis* bonds distributed across two or three octahedra, and for a 1.0 global *cis* fraction, *cis* bonds are usually distributed across all octahedra in the anion ordering. In general, anion orderings with zero or one *cis* octahedra are higher in ground-state energy than those with three or four *cis* octahedra. The anion orderings that are first-, second-, and third-lowest in ground-state energy each have three *cis* octahedra. The final and most important observation is that for each of the 16 cation pairs used for anion ordering analysis, the lowest-energy anion ordering always has a 100% global fraction of *cis* bonding in M–B–M bonds. No anion ordering with even a single *trans* M–B–M bond surpasses the ground-state stability of an anion ordering with all *cis* M–B–M bonds, even if those *cis* bonds are unevenly distributed among the octahedra.

To restate, we used a heuristic strategy to identify a prototypical anion ordering preferred broadly across a wide range of cation chemistries. We enumerated all 32 possible symmetrically distinct orderings of O and N anions within $\sqrt{2} \times \sqrt{2} \times 2$ supercell. We then evaluated the energy of each anion ordering when separately combined with 16 different cation pairs representative of typical cation charge configurations and chemistries. Based on the averaged ground-state energies of the anion orderings across all 16 cation pairs, we predict anion ordering O_0 as an acceptable prototype for the preferred anion ordering across all cation chemistries. Bond-counting statistics suggest that the prototypical anion ordering must have M–B–M bonds which are always in a *cis* configuration and never in a *trans* configuration. Although other factors such as the octa-

hedral tilt and the particular atomic decoration of each octahedron may influence the energy of each anion ordering and deserve further investigation, the major finding is that a highly *cis* configuration correlates generally with low energy.

3.3 Analysis of Energy Above Hull

Thermodynamic stability can be directly estimated in the absence of experimental data using quantum-mechanical methods. Such calculations can predict the energy above the thermodynamic convex hull, or the thermodynamic driving force (i.e., decomposition energy) for a PON material to decompose to its elements, metal nitride or oxide counterparts, or other products.[37] With 316 unique cation pairs and a prototypical anion ordering identified, we compute the the energy above the convex hull to determine PON structure stability. On a plot of ground-state energy versus material composition, the convex hull is the locus of points representing polymorphs or structures with the lowest energy for a given composition. Materials on or close to the convex hull are less likely to decompose to other products.

We computed the energy above the convex hull for each of our PON materials. Our original set of 316 cation pairs includes the possibility for some cation pairs to have multiple charge configurations due to elements with multiple possible oxidation states. However, plane-wave DFT computations usually consider just the composition of a PON structure without the particular oxidation state of the cations, so our set of 316 unique cation pairs reduces to 295 unique cation compositions. For each of the 295 cation compositions, the cations were combined with the O_0 anion ordering to form a full PON structure. These 295 PON structures are then subjected to bulk geometry relaxation to determine the bulk ground-state energy per atom for each structure. Of these relaxations, 227 converged to perovskite geometry under two or more consecutive combined volume-ionic relaxations. The ground-state energies of these 227 converged structures were then combined with the Materials Project database to calculate each structure's decomposition energy relative to the lowest-energy linear combination of stoichiometrically equivalent decomposition products.

Based on the calculated energies above hull, we classify each material's stability from a DFT and thermodynamic standpoint. **Figure 4** shows the results of energy-above-hull calculations for a selected subset of cation pairs that are inside or near the geometric hull from **Figure 2**. **Table 1** shows the stability classifications of the geometric hull (**Section 3.1**) versus the stability classifications obtained from DFT-based energy-above-hull calculations (**Section 3.3**). Thermodynamic computations place the median energy above hull for metastable inorganic crystalline materials at 15 meV/atom.[12] However, for the subset of nitride compounds, this median is 63 meV/atom, owing to the remarkable stability of the N_2 molecule and its strong triple bond. Because our PON structures contain only A–N, B–N, and O–N nitride bonds, even if they are not triple bonds, we reason that some of these materials may still possess metastability at energies above hull higher than the typical inorganic crystalline thresholds. To focus our study on those compounds most likely to be synthesizable, we adopt conservative cutoffs for defining stable, metastable, and unstable PONs. For an energy above hull E_{hull}, we define $0 < E_{hull} < 10$ meV/atom as

Table 1. Counts of PONs by geometric hull classification ("Inside geo. hull" and "Outside geo. hull") versus by stability class ("On Hull", "Stable", "Metastable", and "Unstable") derived from energy-above-hull calculations on DFT ground-state energies. "On Hull" refers to a compound having zero energy above the thermodynamic convex hull, not to being on the boundary of the geometric hull.

Stability Class	Num. inside geo. hull	Num. outside geo. hull	All
On Hull ($E = 0$ meV/atom)	9	11	20
Stable ($0 < E < 10$ meV/atom)	27	38	65
Metastable ($10 \leq E < 25$ meV/atom)	37	72	109
Unstable ($E \geq 25$ meV/atom)	7	26	33
All	80	147	227
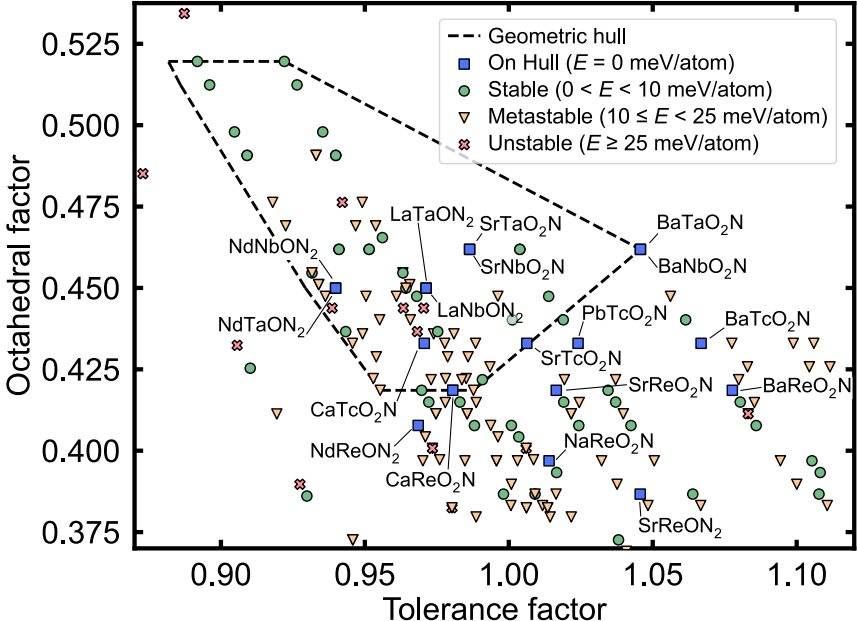
Figure 4. Predicted stability classes for selected PON structures inside or near the geometric hull. Blue squares refer to structures on the thermodynamic convex hull, according to our DFT calculations. Green circles, yellow triangles, and red X marks respectively refer to stable, metastable, and unstable structures, based on decomposition energy ranges as defined in the text. The dotted black line is the geometric hull from **Figure 2**.

stable, 10 meV/atom $\leq E_{\text{hull}} < 25$ meV/atom as metastable, and $E_{\text{hull}} \geq 25$ meV/atom as unstable. $E_{\text{hull}} = 0$ meV/atom signifies materials that are on the thermodynamic convex hull. **Figure 4** shows that a large number of stable materials and materials on the thermodynamic convex hull fall within an approximate $0.95 \leq t \leq 1.07$ and $0.375 \leq \mu \leq 0.475$ window, where t and μ are the Goldschmidt tolerance and octahedral factors, respectively. This window extends outside of the geometric hull, indicating that there may be several potentially promising materials not captured by the geometric hull. Among the compounds predicted to have zero energy above hull are a few known to be synthesizable, including $SrNbO_2N$ and $LaTaON_2$[38–40] as well as $LaNbON_2$, $BaNbO_2N$, $NdNbON_2$, $NdTaON_2$, $SrTaO_2N$, and $BaTaO_2N$.[31]

DFT-derived thermodynamic design rules offer critical additional insight beyond that of the simpler geometric hull. Of the 227 PON structures converged under DFT calculations for which we obtained thermodynamic energies above the convex hull, 85 are classified stable or on-hull, 33 are classified unstable, and the rest are classified metastable (see **Table 1**). For each of the 118 stable, on-hull, and unstable materials, we determined whether the geometric hull predicts that the ma-

terial will form perovskite geometry (i.e., whether the material is plotted inside the geometric hull in **Figure 2**). The geometric hull correlates perovskite geometry with stable/on-hull statuses and non-perovskite geometry with unstable status for only 52.5% of materials. For individual stability classes, the geometric hull predicts perovskite geometry for 45.0% of on-hull materials and 41.5% of stable materials, and non-perovskite geometry for 78.8% of unstable materials. Overall, the geometric hull's prediction of whether a cation chemistry prefers perovskite geometry over other geometry correlates poorly with the calculated thermodynamic stability of that cation chemistry when constrained to a perovskite oxynitride structure. We conclude that in a search for stable PON compounds, the geometric hull approach can initially help exclude unstable candidate materials, but will likely fail to identify many potentially stable materials. Calculating the energy above the thermodynamic convex hull more clearly describes the propensity for a PON solid to remain stable and the degree to which it resists decomposition into thermodynamically competing material phases than if we were to rely on simpler, more common structure rules such as the Goldschmidt tolerance and octahedral factors.

Figure 5 shows the decomposition enthalpy of each perovskite oxynitride structure with a specific cation pair and the anion ordering for its stoichiometry. Several trends follow from this plot. First, there are more stable or metastable ABO$_2$N compounds than ABON$_2$ compounds. Of the 227 compounds converged under DFT relaxation, 156 are of stoichiometry ABO$_2$N and 71 are of stoichiometry ABON$_2$ (see **Tables S9** and **S10**). The lower count of ABON$_2$ compounds arises from the fact that relatively fewer cation pairs both have geometrically preferred sizes and sum to a +8 cationic charge. Also, the higher N content in ABON$_2$ compounds means that synthesizing them requires very high N chemical potentials, even though N$_2$ is so stable that its standard-state chemical potential is low compared to O$_2$.[41] While 42.3% of the ABO$_2$N compounds are classified as stable, only 26.8% of ABON$_2$ compounds meet this threshold. The trend is reversed for metastable compounds, with 43.0% of ABO$_2$N and 59.2% of ABON$_2$ compounds ranked metastable. However, unstable compounds make up approxi-

mately equal percentages of each stoichiometry class (14.7% and 14.1% for ABO$_2$N and ABON$_2$, respectively).

Second, perovskite stability generally increases as the size of the B-site cation decreases. Many more perovskite oxynitride structures classified as stable or metastable appear on the left sides of both heatmaps than the right sides, corresponding with smaller B-site cations. A recent computational study of perovskite oxides identified a similar trend, predicting that the probability of perovskite oxide formability, even across multiple cation charge configurations, increases when the A-site cation is sufficiently larger than the B-site cation.[35] This observation is consistent with the distribution of points in **Figures 2** and **4**, in which the bulk of stable PON compounds and PON compounds with zero energy above hull are concentrated at higher values of the Goldschmidt tolerance factor (i.e., where A has a higher ionic radius compared to B). Additionally, the study also found the effect to be enhanced for A^{III} cation pairs over A^{II} and A^{II} cation pairs. Interestingly, our data show dif-
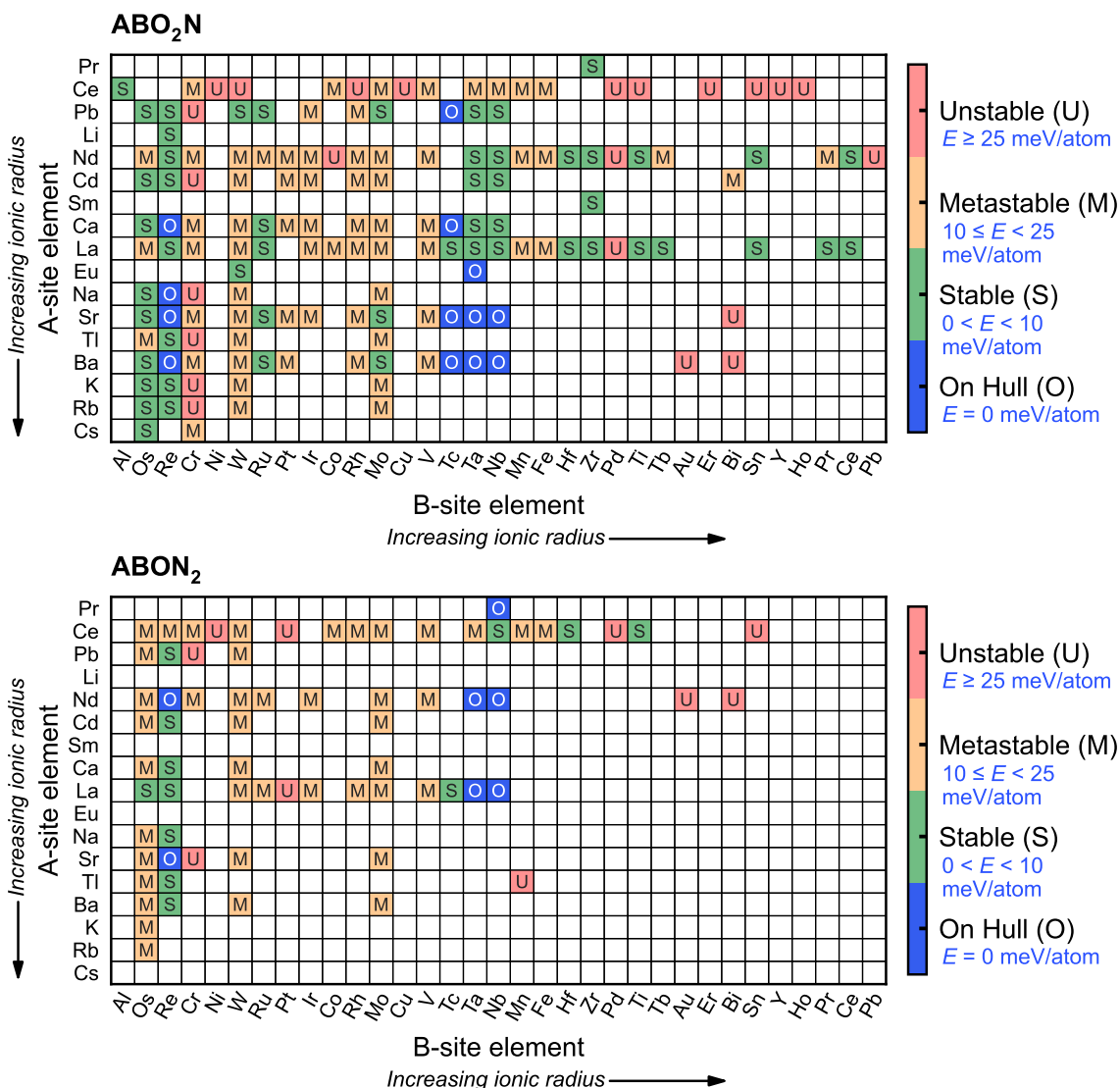

Figure 5. Heat map showing energy above hull for different cation pairs. Blue, green, yellow, and red, cells respectively indicate PON compounds classified as on-hull, stable, metastable, and unstable, based on decomposition energy ranges as defined in the text. White cells indicate cation pairs that are predicted to be highly unstable, not charge-balanced, or do not satisfy basic geometry requirements ($r_A > r_B$). The A- and B-site cations on each axis are arranged in order of increasing nominal ionic radius.[35]

ferent trends, with stable or on-hull PONs dominated by A^{II} compounds (46.3% of all stable or on-hull), followed by A^{III} (36.3%), A^{I} compounds (12.5%), and finally A^{IV} compounds (5.0%) (**Tables S11** and **S12**). Stability appears to be favored when the B-site cation has a more positive charge than the A-site cation does. This may be explained by the need for the B-site cation to coordinate six negatively charged anions while the 12 ions coordinating the A-site cation include a mix of cations and anions. A less positive A-site cation may also have a larger ionic radius, corresponding to the increased stability observed with relatively smaller B-site cations.

Third, perovskite oxynitride structures in which Re is the B-site cation are predicted to be stable, with energies above hull of less than 23 meV/atom across all A-site cations and across both perovskite oxynitride compositions considered. The present work predicts nearly all Re-containing compounds to be stable, in agreement with the conclusion of Wang et al. [7] that Re-containing compounds represent a new class of potentially stable perovskite oxynitrides. A few other material classes, while not as stable as the B = Re class of materials, are potentially promising. Materials with B = Os are nearly all stable for ABO_2N stoichiometry, and nearly all metastable for $ABON_2$ stoichiometry. Similarly, many compounds with B = W and B = Mo for both stoichiometries are predicted to be metastable. These findings agree with a computational study of ternary metal nitrides, which predicted many potentially stable metal nitrides not found in the Inorganic Crystal Structure Database (ICSD). [42] Among the ternary metal nitrides that study proposed for inclusion in the ICSD are compounds containing Re, Os, and Ru, some of which match in metal chemistry with the PONs proposed in this work. Of the stable and on-hull PONs in the present work, 8 with B = Re, 8 with B = Os, and 4 with B = Ru match metal chemistries of proposed stable ternary metal nitrides. If we include metastable PONs, there are 15 with B = Os and also 7 with B = W. Given that the limit of metastability is higher for nitride-containing materials than for inorganic crystalline materials generally, we hypothesize that even the metastable PONs predicted in this work may yet contain synthesizable PON compounds. Additionally, there are many stable and metastable materials of both ABO_2N and $ABON_2$ stoichiometries with $A \in \{Nd, Ca, La, Sr, Ba\}$. In particular, we predict that many A = La and A = Nd compounds will be synthesizable, including B-site cations over a wide range of ionic radii.

Our energy-above-hull calculations have combined 295 unique cation chemistries with a prototypical optimal O_0 anion ordering. 227 of the resulting geometry relaxations converged and were used in combination with data from the Materials Project database to calculate the per-atom energy above the convex hull. In total, we find 85 stable compounds, 109 metastable compounds, and 33 unstable compounds. In particular, we find that cation pairs with $A \in \{La, Pb, Nd, Sr, Ba, Ca\}$ and $B \in \{Re, Os, Nb, Ta\}$ are likely to lead to stable or metastable PON compounds. Counting both metastable and stable PONs in our study as possibly synthesizable (totaling 194), our work may more than triple the number of PONs known to be experimentally synthesizable (i.e., compared to the 68 compounds in Li et al. [31]). The compounds identified could represent new heteroanionic materials for industrial, energy, and environmental materials applications.

3.4 Analysis of Electrochemical Stability

Perovskite oxide materials have been proposed for a number of important electrochemical reactions, such as the oxygen reduction, oxygen evolution, and hydrogen evolution reactions. [43,44] Additionally, PON compounds are likely to catalyze surface reactions via the same types of electrochemical Mars-van Krevelen mechanisms observed in perovskite oxides for oxygen evolution [43] and in metal nitrides for ammonia synthesis. [3] Thus, understanding a PON's electrochemical stability in addition to its thermodynamic stability is necessary to determine the PON's practical usability as an electrocatalyst. Pourbaix diagrams help predict whether a certain set of operating conditions—an operating pH, applied electrical potential—is capable of maintaining the PON in its solid state rather than promoting decomposition to competing aqueous, solid, or gaseous phases. [45] For example, the oxygen evolution reaction in acidic media often requires applied potentials of 2.0 V vs. RHE or higher for practical operation, [46] many transition metal nitrides (such as Mo, Fe, V, and Ni nitrides) are solid in acidic media only for potentials more negative than 0 V vs. SHE. [47] Transition metal nitrides may have more stability as acidic-media ammonia synthesis catalysts, where more negative applied potentials promote higher surface coverage of protons. [3] Additionally, one may generate stability processing diagrams, which show regions of stability similar to a Pourbaix diagram, but in terms of two or more element activities instead of an electrical potential. [48,49] Stability processing diagrams help identify the concentrations of species necessary to keep a phase stable. Beyond knowing a PON is thermodynamically stable outside of solution, Pourbaix and stability processing diagrams can help predict the conditions in which it will remain stable.

To this end, we compute multidimensional Pourbaix and stability process diagrams to understand the operating conditions under which two candidate PON compounds would remain in a stable solid phase. [29,50] Multicomponent Pourbaix diagrams have been used to study quaternary systems such as metal oxychalcogenides,. [51] However, these diagrams are often constructed by solving the Nernst equation to draw phase boundaries between competing phases, an approach that cannot consider the free energy or concentration of each species individually. In contrast, our computational Pourbaix diagrams are derived using a thermodynamic grand potential for each species, which enables us to consider the energy contributions of both ion concentration and chemical potential for all elements. [28] To the best of our knowledge, this work represents the first time this method has been applied to quaternary oxynitride systems. Our high-dimensional Pourbaix diagrams represent an approach beyond what is possible with currently available materials informatics software packages.

We focus on two candidate PON compounds, $CaReO_2N$ and $LaTaON_2$, which were predicted in the previous step to have zero energy above the thermodynamic convex hull. **Figure 6** shows Pourbaix diagrams for these two compounds. For such quaternary systems, the Pourbaix diagram has five dimensions: pH (linked to the chemical potential of O through water equilibrium), the redox potential E, and the chemical potentials of N, A-site cations, and B-site cations. The panels of **Figure 6** show two- or three-dimensional slices of this five-dimensional diagram. Note that standard Pourbaix diagrams are plotted at
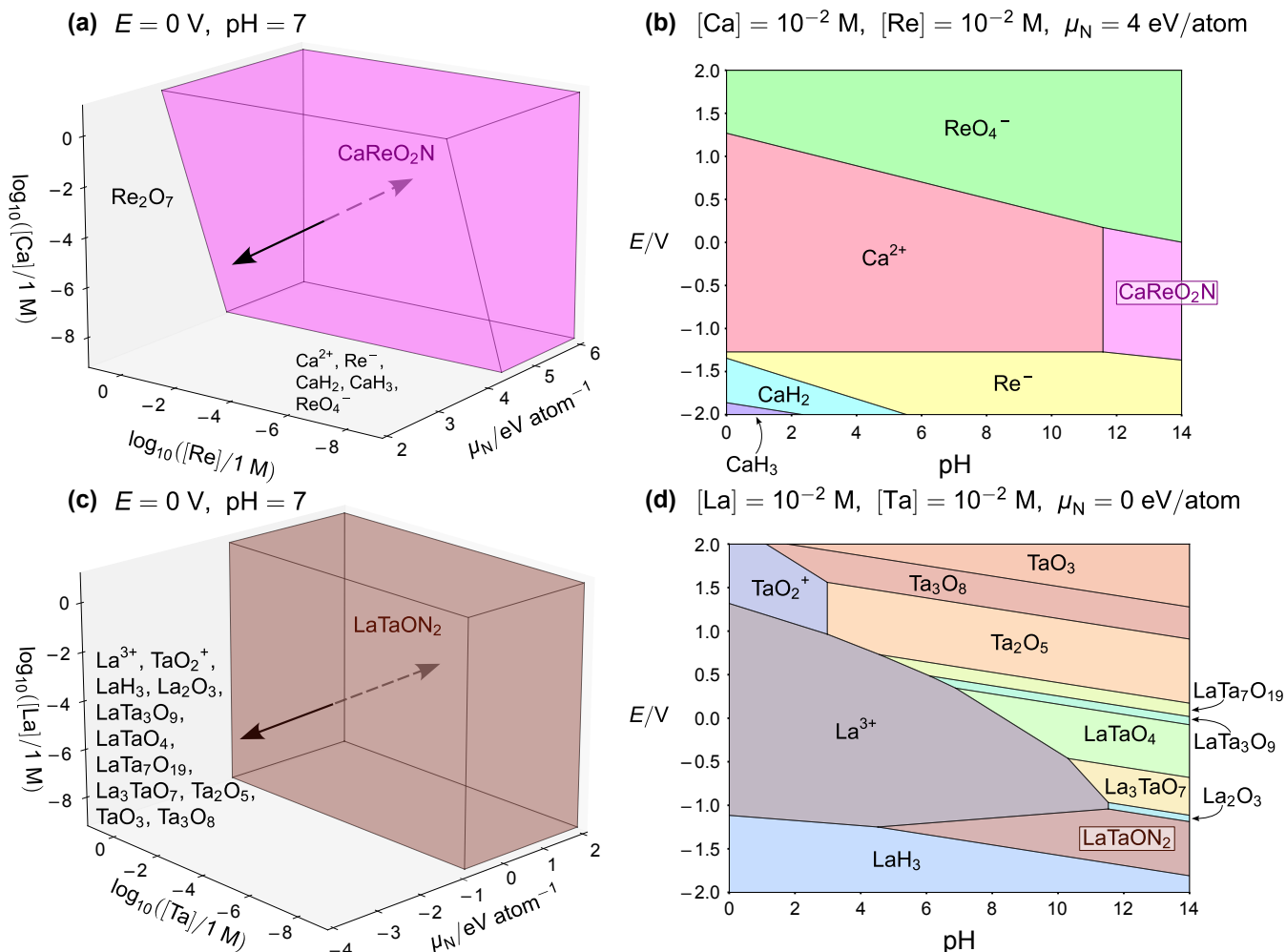
Figure 6. Computational stability processing and Pourbaix diagrams for CaReO$_2$N and LaTaON$_2$. Selected projections of the 5D phase diagram for **(a, b)** CaReO$_2$N and **(c, d)** LaTaON$_2$. **(a, c)** Stability processing diagrams in terms of A- and B-site ion concentration and N chemical potential. For simplicity, only the region corresponding to the solid oxynitride is shown, with other possible decomposition products written outside this region. Arrows indicate changes in N chemical potential (with dashed arrows inside of the solid oxynitride region). **(b, d)** 2D Pourbaix projections of the 5D phase diagram, in terms of E and pH. Potentials are given in V vs. SHE. The boxed compound indicates the solid oxynitride. In all panels, neutral compounds are solid and ionic species are aqueous.

ion concentrations of 10^{-6} mol/L $= 10^{-6}$ M, below the concentration at which a solid oxynitride might crystallize in solution. In this work, we express the A- and B-site chemical potentials as concentrations in **Figure 6a, c**, and plot **Figure 6b, d** at a higher ion concentration of 10^{-2} M.

Figure 6a, c illustrates the ion concentrations and N chemical potentials at which the oxynitride remains solid, as well as other phases that compete at lower metal, O, and N chemical potentials. For both CaReO$_2$N and LaTaON$_2$, stability is generally independent of the B-site ion concentration but depends strongly on N chemical potential. For CaReO$_2$N, solid stability is favored at higher Ca concentrations, but can be achieved at lower Ca concentrations if the N chemical potential is higher. For both compounds, higher N chemical potentials favor the formation of the solid oxynitride over hydride or oxide species. **Figure 6b, d** shows that the solid oxynitride generally forms only under reducing and alkaline conditions. In particular, even at the very high N chemical potential of 4 eV/atom, solid CaReO$_2$N would be usable only for reactions in very alkaline pH ≥ 12 environments. In contrast, LaTaON$_2$

at $\mu_N = 0$ eV/atom has a much wider stability region that extends into acidic conditions, almost to pH $= 4$, but at the cost of requiring more negative applied potentials. Thus, LaTaON$_2$ might be usable in alkaline, neutral, or slightly acidic environments.

Figure 6a shows that the formation of CaReNO$_2$ is likely impossible in water, as CaReNO$_2$ can be stabilized only under conditions where the N chemical potential exceeds ≈ 3.2 eV/atom. Note that even plasma-cracked atomic nitrogen yields a N chemical potential of only $+1$ eV/atom,[52] which means it is highly improbable that an aqueous nitrogen precursor can attain the necessary N chemical potential required to form solid CaReO$_2$N. However, solid LaTaON$_2$ might be synthesized in an aqueous environment, as **Figure 6c** indicates stability of the solid PON at a N chemical potential of only -1 eV/atom, suggesting that the solid oxynitride might be stable in the aqueous state using nitrogen-rich precursors such as urea,[53] ammonia,[54] hydrazine,[55] or melamine.[56,57] Indeed, multiple experimental studies report successful laboratory synthesis of LaTaON$_2$ or LaTaO$_2$N and confirm that this oxynitride does

crystallize in a perovskite structure.[38,58] Despite the lack of established benchmarking for their aqueous chemical potentials, such precursors have demonstrated efficacy in the synthesis of other nitrides and oxynitrides,[56,59] suggesting their potential utility as precursors for the synthesis of PONs.

Our electrochemical analysis shows that a solid PON compound having zero energy above the thermodynamic hull according to DFT calculations may still require special operating conditions to be synthesizable or remain stable in aqueous solution. The energy above hull is useful for quickly screening many PON candidate compounds. However, further stability analysis via ab initio thermodynamics and experimental studies is needed to confirm the synthesizability and long-term stability of a given PON compound under a certain set of operating conditions. Tools such as many-component Pourbaix diagrams can focus high-throughput screening studies on just those candidates that are possible to synthesize at all.

4 Conclusion

We computationally investigate the thermodynamic stability and anion ordering of 156 ABO_2N and 71 $ABON_2$ perovskite oxynitride compounds using density functional theory calculations and Materials Project data.[21] We identify a prototypical anion ordering that is lowest in energy on average across 16 cation chemistries and five charge configurations. This prototypical anion ordering contains exclusively *cis* bonds connecting the B-site cation and the minority-composition anions, similar to that of metal oxysulfides.[14]

Based on our screening calculations, we predict 85 PON compounds to be stable (i.e., energies above hull of 10 meV/atom or less), of which 8 have already been demonstrated stable under laboratory conditions.[31] These 85 stable compounds include PONs with A $\in$ {La, Pb, Nd, Sr, Ba, Ca} and B $\in$ {Re, Os, Nb, Ta}. We predict that these PONs, in addition to the class of Re-containing compounds,[7] will also be experimentally stable.

We generate computational Pourbaix diagrams for the $CaReO_2N$ and $LaTaON_2$ stable candidate materials, which reveal that some materials with zero energy above hull still differ significantly in the range of chemical potential conditions that allow for the PON compound to remain solid. Specifically, $CaReO_2N$ is likely not stable under any practically accessible electrochemical conditions, characterized by an unphysically high required N chemical potential. In contrast, $LaTaON_2$ has a much wider region of operating conditions that could potentially allow for solid stability in an alkaline, reducing environment. Ab initio thermodynamics and experiments are necessary to verify the stability of the proposed stable PONs in this study.

Our work has relevance beyond the question of whether a particular PON compound is stable. Many of the stable and metastable PONs identified in our study may be useful for electrocatalytic, photocatalytic, and photovoltaic applications. Additionally, the concept of enumerating classes of potentially stable PON materials by A- and B-site cation could be used to screen other compounds with similar compositional variability, such as double perovskites, layered perovskites, and spinels.

References

(1) Kageyama, H.; Hayashi, K.; Maeda, K.; Attfield, J. P.; Hiroi, Z.; Rondinelli, J. M.; Poeppelmeier, K. R. Expanding Frontiers in Materials Chemistry and Physics with Multiple Anions. *Nature Communications* **2018**, *9*, 772, DOI: 10.1038/s41467-018-02838-4.

(2) Harada, J. K.; Charles, N.; Poeppelmeier, K. R.; Rondinelli, J. M. Heteroanionic Materials by Design: Progress Toward Targeted Properties. *Advanced Materials* **2019**, *31*, 1805295, DOI: 10.1002/adma.201805295.

(3) Young, S. D.; Ceballos, B. M.; Banerjee, A.; Mukundan, R.; Pilania, G.; Goldsmith, B. R. Metal Oxynitrides for the Electrocatalytic Reduction of Nitrogen to Ammonia. *The Journal of Physical Chemistry C* **2022**, *126*, 12980–12993, DOI: 10.1021/acs.jpcc.2c02816.

(4) Ho-Baillie, A. W. Y.; Zheng, J.; Mahmud, M. A.; Ma, F.-J.; McKenzie, D. R.; Green, M. A. Recent Progress and Future Prospects of Perovskite Tandem Solar Cells. *Applied Physics Reviews* **2021**, *8*, 041307, DOI: 10.1063/5.0061483.

(5) Wang, Z.; Huang, H.; Li, G.; Yan, X.; Yu, Z.; Wang, K.; Wu, Y. Advances in Engineering Perovskite Oxides for Photochemical and Photoelectrochemical Water Splitting. *Applied Physics Reviews* **2021**, *8*, 021320, DOI: 10.1063/5.0039197.

(6) Liu, X.-K.; Xu, W.; Bai, S.; Jin, Y.; Wang, J.; Friend, R. H.; Gao, F. Metal Halide Perovskites for Light-Emitting Diodes. *Nature Materials* **2021**, *20*, 10–21, DOI: 10.1038/s41563-020-0784-7.

(7) Wang, H.-C.; Schmidt, J.; Botti, S.; L. Marques, M. A. A High-Throughput Study of Oxynitride, Oxyfluoride and Nitrofluoride Perovskites. *Journal of Materials Chemistry A* **2021**, *9*, 8501–8513, DOI: 10.1039/D0TA10781F.

(8) Ologunagba, D.; Kattel, S. Transition Metal Oxynitride Catalysts for Electrochemical Reduction of Nitrogen to Ammonia. *Materials Advances* **2021**, *2*, 1263–1270, DOI: 10.1039/D0MA00849D.

(9) Sawada, K.; Nakajima, T. High-Throughput Screening of Perovskite Oxynitride and Oxide Materials for Visible-Light Photocatalysis. *APL Materials* **2018**, *6*, 101103, DOI: 10.1063/1.5041784.

(10) Nayak, P. K.; Mahesh, S.; Snaith, H. J.; Cahen, D. Photovoltaic Solar Cell Technologies: Analysing the State of the Art. *Nature Reviews Materials* **2019**, *4*, 269–285, DOI: 10.1038/s41578-019-0097-0.

(11) Perera, S.; Hui, H.; Zhao, C.; Xue, H.; Sun, F.; Deng, C.; Gross, N.; Milleville, C.; Xu, X.; Watson, D. F.; Weinstein, B.; Sun, Y.-Y.; Zhang, S.; Zeng, H. Chalcogenide Perovskites – an Emerging Class of Ionic Semiconductors. *Nano Energy* **2016**, *22*, 129–135, DOI: 10.1016/j.nanoen.2016.02.020.

(12) Sun, W.; Dacek, S. T.; Ong, S. P.; Hautier, G.; Jain, A.; Richards, W. D.; Gamst, A. C.; Persson, K. A.; Ceder, G. The Thermodynamic Scale of Inorganic Crystalline Metastability. *Science Advances* **2016**, *2*, e1600225, DOI: 10.1126/sciadv.1600225.

(13) Yang, M.; Oró-Solé, J.; Rodgers, J. A.; Jorge, A. B.; Fuertes, A.; Attfield, J. P. Anion Order in Perovskite Oxynitrides. *Nature Chemistry* **2011**, *3*, 47–52, DOI: 10.1038/nchem.908.

(14) Pilania, G.; Ghosh, A.; Hartman, S. T.; Mishra, R.; Stanek, C. R.; Uberuaga, B. P. Anion Order in Oxysulfide Perovskites: Origins and Implications. *npj Computational Materials* **2020**, *6*, 1–11, DOI: 10.1038/s41524-020-0338-1.

(15) Kresse, G.; Furthmüller, J. Efficiency of Ab-Initio Total Energy Calculations for Metals and Semiconductors Using a Plane-Wave Basis Set. *Computational Materials Science* **1996**, *6*, 15–50, DOI: 10.1016/0927-0256(96)00008-0.

(16) Kresse, G.; Furthmüller, J. Efficient Iterative Schemes for *Ab Initio* Total-Energy Calculations Using a Plane-Wave Basis Set. *Physical Review B* **1996**, *54*, 11169–11186, DOI: 10.1103/PhysRevB.54.11169.

(17) Kresse, G.; Hafner, J. *Ab Initio* Molecular Dynamics for Liquid Metals. *Physical Review B* **1993**, *47*, 558–561, DOI: 10.1103/PhysRevB.47.558.

(18) Kresse, G.; Hafner, J. *Ab Initio* Molecular-Dynamics Simulation of the Liquid–Metal–Amorphous–Semiconductor Transition in Germanium. *Physical Review B* **1994**, *49*, 14251–14269, DOI: 10.1103/PhysRevB.49.14251.

(19) Larsen, A. H. et al. The Atomic Simulation Environment—a Python Library for Working with Atoms. *Journal of Physics: Condensed Matter* **2017**, *29*, 273002, DOI: 10.1088/1361-648X/aa680e.

(20) Ong, S. P.; Richards, W. D.; Jain, A.; Hautier, G.; Kocher, M.; Cholia, S.; Gunter, D.; Chevrier, V. L.; Persson, K. A.; Ceder, G. Python Materials Genomics (Pymatgen): A Robust, Open-Source Python Library for Materials Analysis. *Computational Materials Science* **2013**, *68*, 314–319, DOI: 10.1016/j.commatsci.2012.10.028.

(21) Jain, A.; Ong, S. P.; Hautier, G.; Chen, W.; Richards, W. D.; Dacek, S.; Cholia, S.; Gunter, D.; Skinner, D.; Ceder, G.; Persson, K. A. Commentary: The Materials Project: A Materials Genome Approach to Accelerating Materials Innovation. *APL Materials* **2013**, *1*, 011002, DOI: 10.1063/1.4812323.

(22) Blöchl, P. E. Projector Augmented–Wave Method. *Physical Review B* **1994**, *50*, 17953–17979, DOI: 10.1103/PhysRevB.50.17953.

(23) Kresse, G.; Joubert, D. From Ultrasoft Pseudopotentials to the Projector Augmented-Wave Method. *Physical Review B* **1999**, *59*, 1758–1775, DOI: 10.1103/PhysRevB.59.1758.

(24) Perdew, J. P.; Burke, K.; Ernzerhof, M. Generalized Gradient Approximation Made Simple. *Physical Review Letters* **1996**, *77*, 3865–3868, DOI: 10.1103/PhysRevLett.77.3865.

(25) Wang, A.; Kingsbury, R.; McDermott, M.; Horton, M.; Jain, A.; Ong, S. P.; Dwaraknath, S.; Persson, K. A. A Framework for Quantifying Uncertainty in DFT Energy Corrections. *Scientific Reports* **2021**, *11*, 15496, DOI: 10.1038/s41598-021-94550-5.

(26) Jain, A.; Hautier, G.; Ong, S. P.; Moore, C. J.; Fischer, C. C.; Persson, K. A.; Ceder, G. Formation Enthalpies by Mixing GGA and GGA +*U*. *Physical Review B* **2011**, *84*, 045115, DOI: 10.1103/PhysRevB.84.045115.

(27) Hart, G. L. W.; Nelson, L. J.; Forcade, R. W. Generating Derivative Structures at a Fixed Concentration. *Computational Materials Science* **2012**, *59*, 101–107, DOI: 10.1016/j.commatsci.2012.02.015, software available at https://github.com/msg-byu/enumlib, commit e780a44e.

(28) Sun, W.; Kitchaev, D. A.; Kramer, D.; Ceder, G. Non-Equilibrium Crystallization Pathways of Manganese Oxides in Aqueous Solution. *Nature Communications* **2019**, *10*, 573, DOI: 10.1038/s41467-019-08494-6.

(29) Patel, A. M.; Nørskov, J. K.; Persson, K. A.; Montoya, J. H. Efficient Pourbaix Diagrams of Many-Element Compounds. *Physical Chemistry Chemical Physics* **2019**, *21*, 25323–25327, DOI: 10.1039/C9CP04799A.

(30) Persson, K. A.; Waldwick, B.; Lazic, P.; Ceder, G. Prediction of Solid–Aqueous Equilibria: Scheme to Combine First-Principles Calculations of Solids with Experimental Aqueous States. *Physical Review B* **2012**, *85*, 235438, DOI: 10.1103/PhysRevB.85.235438.

(31) Li, W.; Ionescu, E.; Riedel, R.; Gurlo, A. Can We Predict the Formability of Perovskite Oxynitrides from Tolerance and Octahedral Factors? *Journal of Materials Chemistry A* **2013**, *1*, 12239, DOI: 10.1039/c3ta10216e.

(32) Goldschmidt, V. M. Die Gesetze der Krystallochemie. *Naturwissenschaften* **1926**, *14*, 477–485, DOI: 10.1007/BF01507527.

(33) Li, C.; Soh, K. C. K.; Wu, P. Formability of ABO_3 Perovskites. *Journal of Alloys and Compounds* **2004**, *372*, 40–48, DOI: 10.1016/j.jallcom.2003.10.017.

(34) Uchino, K. Functional and Smart Materials: Structural Evolution and Structure Analysis, by Zhong Lin Wang and Zhen Chuan Kang. *Physics Today* **1998**, *51*, 70, DOI: 10.1063/1.882083.

(35) Bartel, C. J.; Sutton, C.; Goldsmith, B. R.; Ouyang, R.; Musgrave, C. B.; Ghiringhelli, L. M.; Scheffler, M. New Tolerance Factor to Predict the Stability of Perovskite Oxides and Halides. *Science Advances* **2019**, *5*, eaav0693, DOI: 10.1126/sciadv.aav0693.

(36) Madelung, E. Das elektrische Feld in Systemen von regelmäßig angeordneten Punktladungen. *19*, 524–533.

(37) Ong, S. P.; Wang, L.; Kang, B.; Ceder, G. Li–Fe–P–O_2 Phase Diagram from First Principles Calculations. *Chemistry of Materials* **2008**, *20*, 1798–1807, DOI: 10.1021/cm702327g.

(38) Bubeck, C.; Widenmeyer, M.; Richter, G.; Coduri, M.; Goering, E.; Yoon, S.; Weidenkaff, A. Tailoring of an Unusual Oxidation State in a Lanthanum Tantalum(IV) Oxynitride via Precursor Microstructure Design. *Communications Chemistry* **2019**, *2*, 1–10, DOI: 10.1038/s42004-019-0237-x.

(39) Kim, Y.-I.; Woodward, P. M.; Baba-Kishi, K. Z.; Tai, C. W. Characterization of the Structural, Optical, and Dielectric Properties of Oxynitride Perovskites AMO_2N (A = Ba, Sr, Ca; M = Ta, Nb). *Chemistry of Materials* **2004**, *16*, 1267–1276, DOI: 10.1021/cm034756j.

(40) Yang, Q.; Masubuchi, Y.; Higuchi, M. Synthesis of Perovskite-Type Oxynitrides $SrNb(O,N)_3$ and $CaTa(O,N)_3$ Using Carbon Nitride. *Ceramics International* **2020**, *46*, 13941–13944, DOI: 10.1016/j.ceramint.2020.02.191.

(41) Zakutayev, A. Design of Nitride Semiconductors for Solar Energy Conversion. *Journal of Materials Chemistry A* **2016**, *4*,

6742–6754, DOI: 10.1039/C5TA09446A.

(42) Sun, W.; Bartel, C. J.; Arca, E.; Bauers, S. R.; Matthews, B.; Orvañanos, B.; Chen, B.-R.; Toney, M. F.; Schelhas, L. T.; Tumas, W.; Tate, J.; Zakutayev, A.; Lany, S.; Holder, A. M.; Ceder, G. A Map of the Inorganic Ternary Metal Nitrides. *Nature Materials* **2019**, *18*, 732–739, DOI: 10.1038/s41563-019-0396-2.

(43) Beall, C. E.; Fabbri, E.; Schmidt, T. J. Perovskite Oxide Based Electrodes for the Oxygen Reduction and Evolution Reactions: The Underlying Mechanism. *ACS Catalysis* **2021**, *11*, 3094–3114, DOI: 10.1021/acscatal.0c04473.

(44) Zhang, M.; Jeerh, G.; Zou, P.; Lan, R.; Wang, M.; Wang, H.; Tao, S. Recent Development of Perovskite Oxide-Based Electrocatalysts and Their Applications in Low to Intermediate Temperature Electrochemical Devices. *Materials Today* **2021**, *49*, 351–377, DOI: 10.1016/j.mattod.2021.05.004.

(45) Delahay, P.; Pourbaix, M.; Van Rysselberghe, P. Potential–pH Diagrams. *Journal of Chemical Education* **1950**, *27*, 683, DOI: 10.1021/ed027p683.

(46) Millet, P. In *Electrochemical Power Sources: Fundamentals, Systems, and Applications*; Smolinka, T., Garche, J., Eds.; Elsevier, 2022; pp 37–62, DOI: 10.1016/B978-0-12-819424-9.00002-1.

(47) Matanovic, I.; Garzon, F. H. Assessing Stability of Transition Metal Nitrides in Aqueous Environments: The Case of Molybdenum, Iron, Vanadium and Nickel Nitride. *Journal of The Electrochemical Society* **2020**, *167*, 046518, DOI: 10.1149/1945-7111/ab7a8b.

(48) Anderko, A.; Sanders, S. J.; Young, R. D. Real-Solution Stability Diagrams: A Thermodynamic Tool for Modeling Corrosion in Wide Temperature and Concentration Ranges. *Corrosion* **1997**, *53*, 43–53, DOI: 10.5006/1.3280432.

(49) Lencka, M. M.; Riman, R. E. Thermodynamic Modeling of Hydrothermal Synthesis of Ceramic Powders. *Chemistry of Materials* **1993**, *5*, 61–70, DOI: 10.1021/cm00025a014.

(50) Zeng, Z.; Chan, M. K. Y.; Zhao, Z.-J.; Kubal, J.; Fan, D.; Greeley, J. Towards First Principles-Based Prediction of Highly Accurate Electrochemical Pourbaix Diagrams. *The Journal of Physical Chemistry C* **2015**, *119*, 18177–18187, DOI: 10.1021/acs.jpcc.5b03169.

(51) Walters, L. N.; Zhang, C.; Dravid, V. P.; Poeppelmeier, K. R.; Rondinelli, J. M. First-Principles Hydrothermal Synthesis Design to Optimize Conditions and Increase the Yield of Quaternary Heteroanionic Oxychalcogenides. *Chemistry of Materials* **2021**, *33*, 2726–2741, DOI: 10.1021/acs.chemmater.0c02682.

(52) Caskey, C. M.; Richards, R. M.; Ginley, D. S.; Zakutayev, A. Thin Film Synthesis and Properties of Copper Nitride, a Metastable Semiconductor. *Materials Horizons* **2014**, *1*, 424–430, DOI: 10.1039/C4MH00049H.

(53) Okada, R.; Katagiri, K.; Masubuchi, Y.; Inumaru, K. Preparation of $LaTiO_2N$ Using Hydrothermally Synthesized $La_2Ti_2O_7$ as a Precursor and Urea as a Nitriding Agent. *European Journal of Inorganic Chemistry* **2019**, *2019*, 1257–1264, DOI: 10.1002/ejic.201801526.

(54) Clarke, S. J.; Guinot, B. P.; Michie, C. W.; Calmont, M. J. C.; Rosseinsky, M. J. Oxynitride Perovskites: Synthesis and Structures of $LaZrO_2N$, $NdTiO_2N$, and $LaTiO_2N$ and Comparison with Oxide Perovskites. *Chemistry of Materials* **2002**, *14*, 288–294, DOI: 10.1021/cm010577v.

(55) Brayner, R.; Djéga-Mariadassou, G.; Marques da Cruz, G.; Rodrigues, J. A. J. Hydrazine Decomposition over Niobium Oxynitride with Macropores Generation. *Catalysis Today* **2000**, *57*, 225–229, DOI: 10.1016/S0920-5861(99)00330-2.

(56) Ashraf, I.; Rizwan, S.; Iqbal, M. A Comprehensive Review on the Synthesis and Energy Applications of Nano-Structured Metal Nitrides. *Frontiers in Materials* **2020**, *7*, DOI: 10.3389/fmats.2020.00181.

(57) Kitano, M.; Kujirai, J.; Ogasawara, K.; Matsuishi, S.; Tada, T.; Abe, H.; Niwa, Y.; Hosono, H. Low-Temperature Synthesis of Perovskite Oxynitride-Hydrides as Ammonia Synthesis Catalysts. *Journal of the American Chemical Society* **2019**, *141*, 20344–20353, DOI: 10.1021/jacs.9b10726.

(58) Wang, Y.; Kang, Y.; Zhu, H.; Liu, G.; Irvine, J. T. S.; Xu, X. Perovskite Oxynitride Solid Solutions of $LaTaON_2$–$CaTaO_2N$ with Greatly Enhanced Photogenerated Charge Separation for Solar-Driven Overall Water Splitting. *Advanced Science* **2021**, *8*, 2003343, DOI: 10.1002/advs.202003343.

(59) Sun, W.; Holder, A.; Orvañanos, B.; Arca, E.; Zakutayev, A.; Lany, S.; Ceder, G. Thermodynamic Routes to Novel Metastable Nitrogen-Rich Nitrides. *Chemistry of Materials* **2017**, *29*, 6936–6946, DOI: 10.1021/acs.chemmater.7b02399.

(A) (B) (O) (N)   (M) Minority-composition anion

ABO$_2$N, ABON$_2$

M–B–M
cis bond

log$_{10}$([A]/ 1 M)
0
−2
−4
−6
−8

Region of oxynitride stability

log$_{10}$([B]/1 M)
0 −2 −4 −6 −8
−4 −3 −2 −1 0 1 2
μ_N/eV atom^{-1}
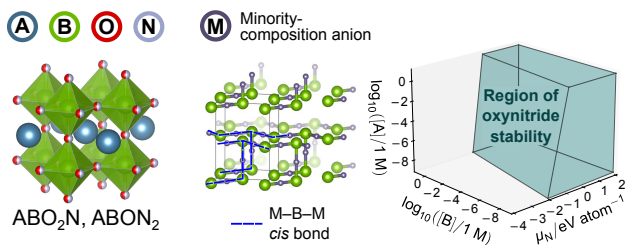
A ∈ {La, Pb, Nd, Sr, Ba, Ca}
B ∈ {Re, Os, Nb, Ta}

Preferred ordering has 100% *cis* M–B–M bonding

Pourbaix diagrams predict conditions for aqueous stability

(For Table of Contents Only.)